Optical properties of stacked liquid crystal superstructures with opposite chirality [Invited]

Lin Zhu (朱 琳)[†], Yiheng Zhang (张逸恒)[†], Shijun Ge (葛士军), Peng Chen (陈 鹏)[*], and Yanqing Lu (陆延青)

National Laboratory of Solid State Microstructures, Key Laboratory of Intelligent Optical Sensing and Manipulation, College of Engineering and Applied Sciences, and Collaborative Innovation Center of Advanced Microstructures, Nanjing University, Nanjing 210093, China

[†]These authors contributed equally to this work.
*Corresponding author: chenpeng@nju.edu.cn

Cholesteric liquid crystal (CLC) has been widely used in flat optical elements due to the Pancharatnam–Berry (PB) phase modulation. In order to achieve PB phase modulation for both circular polarizations, it is natural to come up with stacking CLCs with opposite chirality. Here, various optical properties of diverse CLC stacking structures are systematically investigated by numerical calculations. With the thickness of the CLC sublayers becoming smaller, the reflection bandgap splits into three main parts, and the rotatory dispersion gradually becomes negligible. Vector beams provide a more intuitive verification. These results provide theoretical guidance for future studies on stacked chiral anisotropic media.

Keywords: cholesteric liquid crystals; Pancharatnam–Berry phases; chirality; vector beams.
DOI: 10.3788/COL202422.061601

1. Introduction

Liquid crystal is known for the combination of the fluidity of liquid and the dielectric anisotropy of crystals. Cholesteric liquid crystal (CLC) is a typical liquid crystalline phase with the helical ordering of anisotropic molecules[1-3]. Rod-like CLC molecules self-assemble into a spiral organization along the helical axis due to the helical twisting power of the chiral monomers. The spiral organization is characterized by a helical pitch p, the distance over which the molecules twist 2π. The CLC exhibits a striking feature—Bragg reflection. Light propagating along the helix axis with the appropriate wavelength (from $n_o p$ to $n_e p$) can be reflected, where n_e and n_o represent extraordinary and ordinary refractive indices, respectively. Moreover, the chiral structure of the CLC endows the Bragg reflection with the spin-selectivity, therein, only light with the same circular polarization chirality as the CLC can be reflected, while the opposite one is transmitted. Such intriguing optical properties have facilitated wide applications in filters, circular polarizers, displays, and lasers[4-7].

In 2016, researchers found light reflected from CLC is endowed with geometric phase, also known as Pancharatnam–Berry phase (PB phase)[8-11], which is determined by the orientation angle of the CLC director at the front surface. Thanks to the CLC alignment techniques with high resolution[12,13], arbitrary PB phase design makes patterned CLCs compelling in flat optics[14-19]. Vortex beam generators, flat lenses, and beam splitters[20-22] are representative CLC PB phase elements[8]. However, the PB phase only exists in reflected light, and the transmitted light remains untailored, so only one of the circular polarizations can be attached with PB phase. Such chirality-selectivity limits the functions of CLC PB phase modulation. Solutions to break this limitation can be summarized into two kinds: spin angular momentum (SAM) reversal[23] and opposite-chirality CLC stacking[24-27]. By adding a mirror at the back of the CLC, the transmitted light with chirality opposite to the CLC will reverse its SAM after specular reflection, and then a PB phase can be attached. The other practical option is stacking CLC layers with right-handedness and left-handedness together so that both circularly polarized light can be Bragg reflected, making conjugated PB phase modulation achievable. Up to now, the cascade of a right-handed and a left-handed CLC devices[25], and a single device consisting of both handedness[24,26,27], have been demonstrated in experiments. For diverse types of CLC stacks, there still lacks a comprehensive model on their optical properties, especially the PB phase, which is very important for taking more profound insight into those observed phenomena and predicting more intriguing properties in some unexplored structures.

In this work, we systematically investigate the optical properties of various stacked liquid crystal superstructures with opposite chirality. We propose a consistent framework to describe the trivial cascade of two CLC structures with opposite chirality, the opposite-chirality-coexisted superstructures, and other intermediate configurations. Through numerical simulations, the reflections from different stacked structures are compared under normal and linearly polarized incidence. Both circular

polarizations can be reflected in these opposite-chirality stacks, and particularly the Bragg bandgap splits when the structural repeating units become thin enough. We also study the reflective PB phase and clarify how the CLC director orientation determines the linear polarization angle of the reflected light. Specifically, the reflected linear polarization also depends on the incident wavelength, attributing to the propagation phase difference between orthogonal circular polarization components. Such rotatory dispersion can be wholly suppressed in the opposite-chirality-coexisted superstructures. In addition to uniform alignment, we further imprint an azimuthally gradient pattern on the CLC stacks and verify the capability of vector beam generation[26,28], indicating the broadband and

left-handed CLC sublayers alternatively in the z-direction. The whole stacking structure can be treated as the repeating of the smallest repeating unit. To be more specific, the repeating unit of thickness A consists of one right-handed sublayer and one left-handed sublayer, and the thickness of each sublayer is $A/2$. Starting from the front surface with the director orientation angle α in the x–y plane, the CLC superstructure rotates in the positive direction (right-handed) within $A/2$ and continues in a left-handed helix within the next $A/2$, and again with right-handedness, and so forth. In this way, a stacked structure with opposite chirality is established with a total thickness D along the z-axis. The dielectric tensor of the stacked CLC model with opposite chirality can be formulated as

$$
\begin{cases}
\boldsymbol{\varepsilon}_R(z) = \begin{bmatrix} \varepsilon_m + \varepsilon_m\delta \cos 2\left(\frac{2\pi}{p}z - \alpha\right) & \varepsilon_m\delta \sin 2\left(\frac{2\pi}{p}z - \alpha\right) & 0 \\ \varepsilon_m\delta \sin 2\left(\frac{2\pi}{p}z - \alpha\right) & \varepsilon_m - \varepsilon_m\delta \cos 2\left(\frac{2\pi}{p}z - \alpha\right) & 0 \\ 0 & 0 & \varepsilon_3 \end{bmatrix}, & (k-1)A \leq z < \left(k - \frac{1}{2}\right)A \\
\boldsymbol{\varepsilon}_L(z) = \begin{bmatrix} \varepsilon_m + \varepsilon_m\delta \cos 2\left(-\frac{2\pi}{p}z - \alpha\right) & \varepsilon_m\delta \sin 2\left(-\frac{2\pi}{p}z - \alpha\right) & 0 \\ \varepsilon_m\delta \sin 2\left(-\frac{2\pi}{p}z - \alpha\right) & \varepsilon_m - \varepsilon_m\delta \cos 2\left(-\frac{2\pi}{p}z - \alpha\right) & 0 \\ 0 & 0 & \varepsilon_3 \end{bmatrix}, & \left(k - \frac{1}{2}\right)A \leq z < kA
\end{cases}, \quad (1)
$$

where $k = 1, 2, \ldots, D/A$.

dispersion-free manipulation of structured light. This work provides a full insight into the optical physics of opposite-chirality CLC superstructures and offers a theoretical guidance on their designs and applications.

2. Results

2.1. Design and principles

Figure 1 illustrates the schematic of four typical types of stacked CLC superstructures, constructed by stacking right-handed and
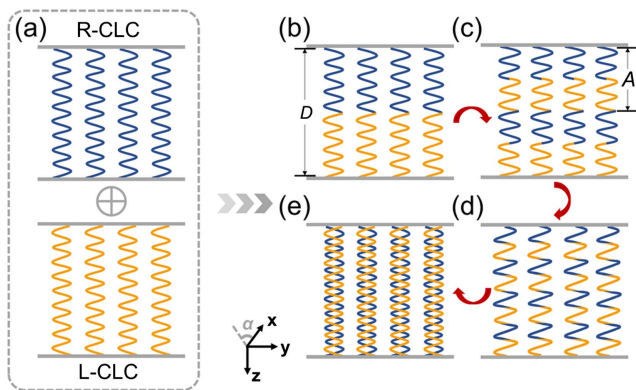

Fig. 1. Schematics of (a) common cholesteric liquid crystals (CLCs) and (b)–(e) four stacked CLC superstructures. The blue and yellow spirals represent right-handed and left-handed CLC, respectively. D means the thickness of the cell. A means the thickness of the smallest repeating unit. The z-axis is along the helical axis.

Here, $\varepsilon_m = (\varepsilon_1 + \varepsilon_2)/2$ and $\delta = (\varepsilon_1 - \varepsilon_2)/(\varepsilon_1 + \varepsilon_2)$. $\varepsilon_1 = n_e^2$ and $\varepsilon_2 = \varepsilon_3 = n_o^2$ are the three principal values. α represents the orientation angle of the CLC director at the front surface (i.e., $z = 0$). The helical axis is along the z-axis, and the local LC director at the surface is parallel to the x–y plane. We keep D constant and change A from dozens of pitches to no more than half of the pitch (p) in order to construct various kinds of stacked superstructures. The value of A indicates the alternating rate of sublayers with opposite chirality. For example, the case of $A = D$ is composed of one layer of right-handed CLC and another layer of left-handed CLC with the same thickness [Fig. 1(b)], while the limiting case of $A \approx 0$ represents the opposite-chirality-coexisted superstructures [Fig. 1(e)].

In order to simulate the optical properties of the aforementioned stacked CLCs, we use the 4×4 matrix algorithm introduced by Berreman and Scheffer[29,30], which is suitable for stratified and anisotropic media. We consider uniformly polarized and normal incidence at the CLCs (i.e., light propagates along the z-axis). According to the Maxwell equations, only four components of the electric and magnetic fields are needed to specify the light, and the Berreman vector is defined as

$$\mathbf{f}(z) = [E_x(z), iH_y(z), E_y(z), -iH_x(z)]^{\mathrm{T}}. \quad (2)$$

From the dielectric tensor between z and $z + \Delta z$, we can calculate the propagation matrix $\mathbf{P}(z, \Delta z)$ satisfying $\mathbf{f}(z + \Delta z) = \mathbf{P}(z, \Delta z)\mathbf{f}(z)$[29-31]. Through multiplying the propagation matrices of single-chirality sublayers in sequence, the total matrix $\mathbf{P}(0, D)$ of the whole CLC is obtained:

$$\mathbf{P}(0, D)$$
$$= \mathbf{P}_L\left(D - \frac{A}{2}, \frac{A}{2}\right)\mathbf{P}_R\left(D - A, \frac{A}{2}\right)\ldots\mathbf{P}_L\left(\frac{A}{2}, \frac{A}{2}\right)\mathbf{P}_R\left(0, \frac{A}{2}\right). \tag{3}$$

Here, $\mathbf{P}_R$ and $\mathbf{P}_L$ correspond to the right-handed and the left-handed sublayers, respectively. By solving the matrix equation $\mathbf{f}_{trans} = \mathbf{P}(0, D)(\mathbf{f}_{inc} + \mathbf{f}_{ref})$, we can calculate the reflected light $\mathbf{f}_{ref}$ and the transmitted light $\mathbf{f}_{trans}$ from the known incident light $\mathbf{f}_{inc}$. Based on this 4×4 matrix algorithm, we investigate the unusual Bragg reflection from the stacked CLC superstructures. The trivial case with uniform surface alignment (i.e., constant α) is studied. Furthermore, we consider the patterned superstructures with $\alpha(x, y)$ variant in the x–y plane. The reflective PB phase modulation from the structured CLCs is a valuable tool for broadband structured light generation. The CLC superstructure with opposite chirality can reflect both circular polarizations, allowing simultaneous PB phase control for both SAM eigenstates[26]. The broadband generation of vector beams is studied as a typical application.

2.2. Optical properties of uniformly aligned CLC stacks

We consider different CLC stacks with $A = D$, $A = D/2$, $A = D/4$, and $A \approx 0$ [Figs. 1(b)–1(e)], as well as the common right-handed CLC for comparison. Their material parameters are $n_e = 1.7$, $n_o = 1.5$, $p = 400$ nm, and $D = 8000$ nm. The linear polarization along the x-axis is selected as the incidence so that the optical response of both right-handed and left-handed circularly polarized components can be revealed. Using the home-made 4×4 matrix solver loaded in MATLAB, we simulate the dependence of the reflected light on two physical quantities, the wavelength λ and the surface director orientation α. For common right-handed CLC, only half of the linearly polarized input light is reflected due to the spin-selective Bragg reflection. As displayed in Fig. 2(a), the modeled Bragg reflection bandgap is approximately 600–680 nm, which corresponds to $n_o p - n_e p$. The phase of the E_x component in the reflected light is plotted in Fig. 2(f), indicating the reflective PB phase of $+2\alpha$. Figure 2(f) also shows that the phase of E_x depends on the input wavelength, which results from the dynamic phase accumulation.

More intriguing properties are discovered in the CLC stacks of opposite chirality. First of all, as shown in Figs. 2(b)–2(e), the reflectance within the Bragg reflection bandgap reaches 100% since both circular polarizations are reflected. It is more interesting that the Bragg bandgap splits into three main parts when $A \leq D/2$, as displayed in Figs. 2(c)–2(e). As A shortens, the central wavelength of the central bandgap stays, while the two side bandgaps gradually shift away from the central bandgap. The locations and the widths of these three main bandgaps can be deduced by Fourier analysis[32,33]. Secondly, the reflected light is linearly polarized, and its polarization angle depends on both λ and α, as vividly illustrated in Figs. 2(g)–2(j). On one hand, for a certain λ, the polarization angle is proportional to α, which means that the rotation of the CLC surface director will cause the rotation of the linear polarization. On the other hand, for a fixed α, the polarization angle varies with λ. As A becomes smaller, such dispersion becomes weaker [Fig. 2(g)–2(i)], and finally in the limiting case of $A \approx 0$ (i.e., opposite-chirality-coexisted superstructure), the polarization angle is independent of λ [Fig. 2(j)].

We can explain the above dependence via the Jones vector calculus[34]. The right-handed/left-handed component is endowed with a PB phase of $\pm 2\alpha$, respectively. Additionally, the left-handed component propagates across the right-handed sublayers before and after getting reflected in the left-handed sublayers, so it undergoes a longer distance than the right-handed component, and an extra dynamic phase ψ is attached. Since the incident polarization is x-directional ($|x\rangle = |\mathbf{R}\rangle + |\mathbf{L}\rangle$), the resultant
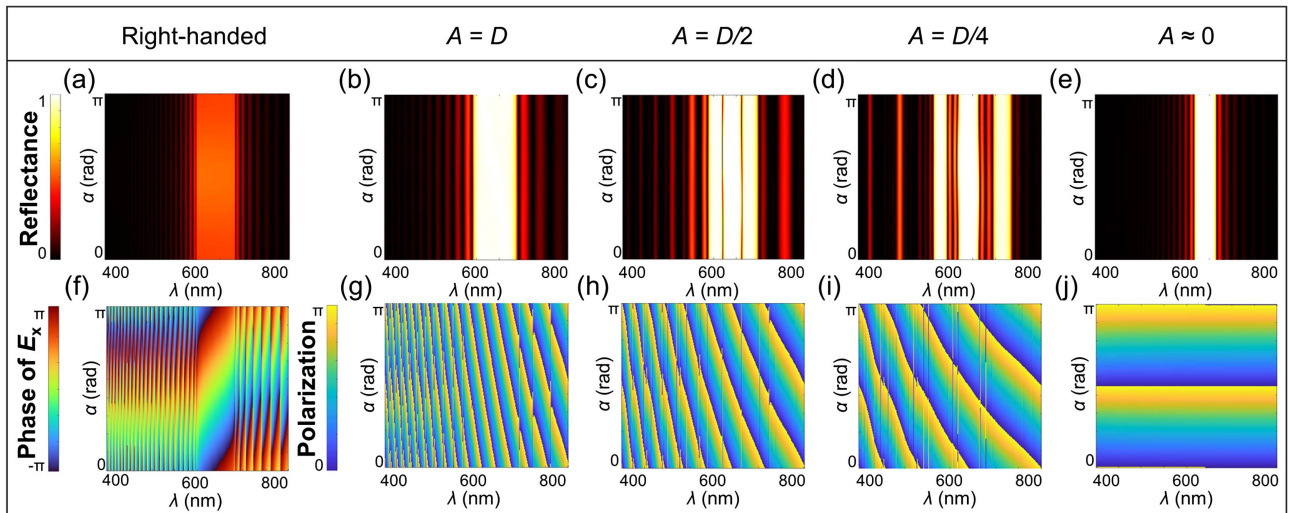

Fig. 2. (a), (f) The reflection spectrum and the phase of E_x component of the light reflected from right-handed CLC. (b)–(e) The reflectance spectra and (g)–(j) the polarization of the light reflected from four stacked CLC models. The stacked CLCs are (b), (g) $A = D$, (c), (h) $A = D/2$, (d), (i) $A = D/4$, and (e), (j) $A \approx 0$, respectively.

reflected light can be deduced as (normalization factors are omitted)

$$|\mathbf{R}\rangle e^{+i2\alpha} + |\mathbf{L}\rangle e^{-i2\alpha+i\psi} = (\hat{x} - i\hat{y})e^{+i2\alpha} + (\hat{x} + i\hat{y})e^{-i2\alpha+i\psi}$$
$$= 2e^{i\psi/2}[\hat{x}\,\cos(2\alpha - \psi/2) + \hat{y}\,\sin(2\alpha - \psi/2)], \qquad (4)$$

which yields the linear polarization at the angle $2\alpha - \psi/2$. Since ψ varies with λ, the reflected polarization rotates at different wavelengths, which is known as reflective rotatory dispersion[27]. Smaller A will reduce ψ, and such rotatory dispersion is fully suppressed in the opposite-chirality-coexisted superstructures with $A \approx 0$ [Fig. 2(j)].

In order to vividly reveal the polarization of the reflected light, we insert an x-directional analyzer in the reflection path, and the analyzed reflectance spectra are simulated in Figs. 3(a)–3(e). The reflectance within the bandgap in Fig. 3(a) reduces to about 25% since half intensity of reflected right-handed circular polarization is blocked. Compared to Figs. 2(b)–2(e) without analyzer, the spectra in Figs. 3(b)–3(e) are sinusoidally modulated. The reflectance reaches its maxima when the reflected polarization is parallel to the analyzer. This condition can be written as $2\alpha - \psi/2 = 0$ (or π), where the dynamic phase retardation ψ depends on the wavelength λ. First, we analyze the effect of λ by taking the section of the analyzed spectra at $\alpha = \pi/2$ [Figs. 3(f)–3(j)]. The oscillations in the reflectance spectra clearly show the wavelength-dependent variation in polarization direction. As expected, rotatory dispersion is not observed in the single-chirality case in Fig. 3(f) and the limiting case in Fig. 3(j) because the reflected light is circularly polarized for common

CLC and $\psi \approx 0$ in the opposite-chirality-coexisted superstructures. Secondly, we take the section at $\lambda = 633$ nm to illustrate the relation between α and the reflected polarization, as shown in Figs. 3(k)–3(o). The reflectance without the analyzer is basically independent of α, and the slight vibration can be explained by the Fabry–Pérot harmonics arising from the air–CLC interface[35]. For opposite-chirality CLC stacks in Figs. 3(l)–3(o), when α ranges from 0 to π, the analyzed reflectance oscillates in the form of $\cos^2(2\alpha - \psi/2)$, reaching its maxima 100% and minima 0% both for two times. This rule agrees with the fact that the reflective PB phase equals $\pm 2\alpha$.

2.3. Vector beams generated from patterned CLC stacks

To verify the capability of structured light generation by the CLC stacks with opposite chirality, we imprint a delicate pattern on the surface directors of the CLC superstructures. As shown in Fig. 4(a), the CLC directors at the front surface should rotate according to $\alpha(x, y) = (M/2) \times \arctan(y/x)$, where M is selected as $+1$. Here, M is the polarization order of the generated cylindrical vector beam, which means that its local polarization orientation rotates $|2\pi M|$ per circulation about the central singularity. We compare the vector beams generated from three cases of CLC stacks, including $A = D$ in Figs. 4(b)–4(e), $A = D/4$ in Figs. 4(f)–4(i), and $A \approx 0$ in Figs. 4(j)–4(m). As shown in Figs. 2(b), 2(d), 2(e) and Figs. 4(c), 4(g), 4(k), the reflectance from CLC stacks is independent of α. As an example, Fig. 4(d) displays the rotating polarization distribution, the donut-shaped spot, and the analyzed intensity profile with two lobes, which verifies the generation of the vector beam with $M = +1$.
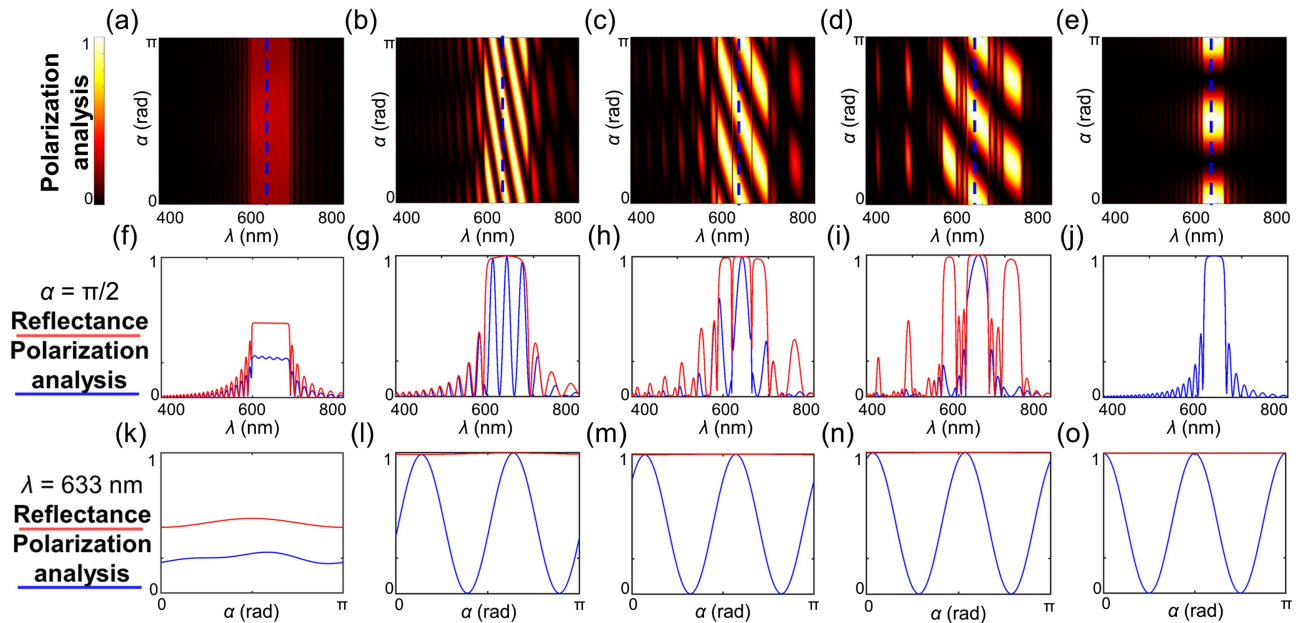

Fig. 3. The optical properties of (a), (f), (k) the right-handed CLC and the stacked CLCs with (b), (g), (l) $A = D$, (c), (h), (m) $A = D/2$, (d), (i), (n) $A = D/4$, and (e), (j), (o) $A \approx 0$, respectively. (a)–(e) The reflectance spectra after an x-directional analyzer dependent on α and λ. (f)–(j) The section at $\alpha = \pi/2$, and (k)–(o) the section at $\lambda = 633$ nm [blue dashed lines in (a)–(e)], where the red/blue curves represent the reflectance without analyzer/with an x-directional analyzer, respectively.
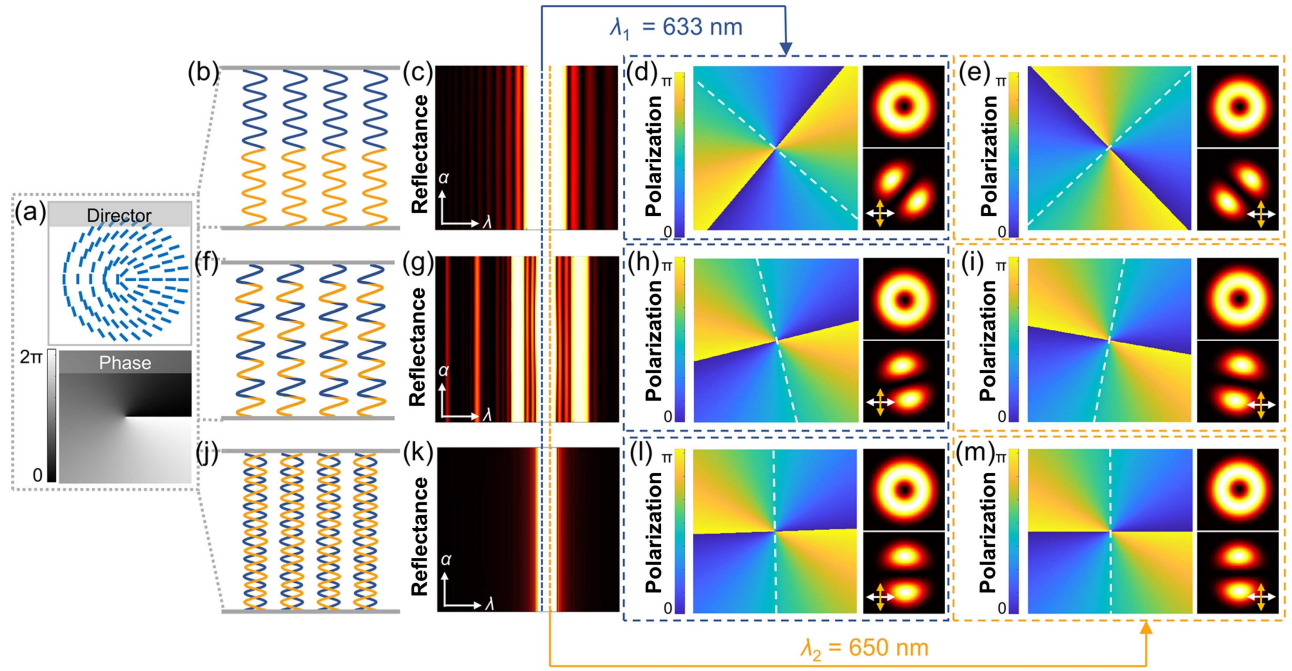
Fig. 4. The polarization distribution and diffracted optical field of the three patterned CLC stacks: (b)–(e) $A = D$, (f)–(i) $A = D/4$, and (j)–(m) $A \approx 0$. (a) The designed surface CLC alignment and phase pattern. (b), (f), (j) Schematics of three stacked CLC models, corresponding to Figs. 1(b), 1(d), 1(e), respectively. (c), (g), (k) Reflectance spectra of the three CLC models corresponding to Figs. 2(b), 2(d), 2(e), respectively. The polarization distribution and the diffracted optical field with/without analyzer for the generated vector beams at (d), (h), (l) 633 nm and (e), (i), (m) 650 nm, respectively. The white/yellow arrows represent the incident polarizer/analyzer, respectively. The white dashed lines indicate the position of $\pi/2$ polarization.

Now we compare two representative incident wavelengths (633 nm and 650 nm) within the central Bragg bandgap. As indicated by Figs. 4(d) and 4(e), at these two incident wavelengths, the vector beams exhibit different polarization distributions and different orientations of the analyzed intensity profile, which is attributed to the evident rotatory dispersion in the cascaded CLC with $A = D$. When we continue to the case of $A = D/4$, the polarization variance between the vector beams becomes smaller [Figs. 4(h) and 4(i)], and finally such variance vanishes in the limiting case of $A \approx 0$ [Figs. 4(l) and 4(m)]. This phenomenon again proves that the reflective rotatory dispersion becomes weaker as A decreases. Importantly, the rotatory dispersion is fully suppressed in the opposite-chirality-coexisted CLC model, owing to the negligible dynamic phase difference between the right-handed and the left-handed circularly polarized components. The above results of the generated vector beams offer a vivid illustration of the PB phase and the rotatory dispersion in the patterned CLC stacks. This implies a promising strategy for broadband and dispersion-free structured light manipulation.

3. Discussion

In this work, we proposed the theoretical models of the opposite-chirality CLC stacked superstructures and developed a 4×4 matrix solver for simulating corresponding optical properties.

The Bragg bandgap will split into three bandgaps if the stacking sublayers become thin enough. This property implies the opportunities of multiple working bands, possibly enabling simultaneous manipulation of red, green, and blue light. The orientation of the reflected linear polarization depends on the surface CLC director and the wavelength, which results from the PB phase and the propagation phase difference of two circularly polarized components. Interestingly, this dispersion can be well controlled by the stacking form of the opposite-chirality CLCs. On one hand, we can make broadband and dispersion-free beam shaping possible in the limiting case of $A \approx 0$. On the other hand, CLC optical elements with designable wavelength dependence can be achieved, e.g., wavelength multiplexed holograms[27]. Furthermore, a vector beam generator by patterned CLC stacks is numerically demonstrated. The proposed theoretical model matches well with the reported experimental results in two extreme cases, namely the two-layer CLC stack $(A = D)$[27] and the opposite-chirality-coexisted superstructures $(A \approx 0)$[26]. Besides, other presented results of intermediate forms provide good predictions on their optical properties and functionalities for light control. It is possible to demonstrate the intermediate configurations via spin-coating technique and polymerizable materials, which are adopted in the fabrication of gradient-pitch CLCs[36,37] and piecewise-twisted CLCs[38]. This work gives deeper understanding of opposite-chirality CLC stacks and promisingly shows theoretical directions for complex chiral anisotropic structures.

References

1. M. Schwartz, G. Lenzini, Y. Geng, *et al.*, "Cholesteric liquid crystal shells as enabling material for information-rich design and architecture," Adv. Mater. **30**, 1707382 (2018).
2. L. Wang, A. M. Urbas, and Q. Li, "Nature-inspired emerging chiral liquid crystal nanostructures: from molecular self-assembly to DNA mesophase and nanocolloids," Adv. Mater. **32**, 1801335 (2020).
3. C. L. Yuan, W. B. Huang, X. Q. Wang, *et al.*, "Electrically tunable helicity of cholesteric heliconical superstructure," Chin. Opt. Lett. **18**, 080005 (2020).
4. Y. H. Ge, Y. M. Lan, X. R. Li, *et al.*, "Polymerized cholesteric liquid crystal microdisks generated by centrifugal microfluidics towards tunable laser emissions," Chin. Opt. Lett. **18**, 080006 (2020).
5. Y. H. Zhang, P. Chen, C. T. Xu, *et al.*, "Dynamically selective and simultaneous detection of spin and orbital angular momenta of light with thermoresponsive self-assembled chiral superstructures," ACS Photonics **9**, 1050 (2022).
6. Y. Cao, L. Chong, K. H. Wu, *et al.*, "Dynamic coloration of polymerized cholesteric liquid crystal networks by infiltrating organic compounds," Chin. Opt. Lett. **20**, 091602 (2022).
7. K. Koshelev, P. Tonkaev, and Y. Kivshar, "Nonlinear chiral metaphotonics: a perspective," Adv. Photonics **5**, 064001 (2023).
8. J. Kobashi, H. Yoshida, and M. Ozaki, "Planar optics with patterned chiral liquid crystals," Nat. Photonics **10**, 389 (2016).
9. M. Rafayelyan, G. Tkachenko, and E. Brasselet, "Reflective spin-orbit geometric phase from chiral anisotropic optical media," Phys. Rev. Lett. **116**, 253902 (2016).
10. R. Barboza, U. Bortolozzo, M. G. Clerc, *et al.*, "Berry phase of light under Bragg reflection by chiral liquid-crystal media," Phys. Rev. Lett. **117**, 053903 (2016).
11. J. Kobashi, H. Yoshida, and M. Ozaki, "Polychromatic optical vortex generation from patterned cholesteric liquid crystals," Phys. Rev. Lett. **116**, 253903 (2016).
12. P. Chen, L. L. Ma, W. Hu, *et al.*, "Chirality invertible superstructure mediated active planar optics," Nat. Commun. **10**, 2518 (2019).
13. Z. X. Li, Y. P. Ruan, P. Chen, *et al.*, "Liquid crystal devices for vector vortex beams manipulation and quantum information applications," Chin. Opt. Lett. **19**, 112601 (2021).
14. N. Yu and F. Capasso, "Flat optics with designer metasurfaces," Nat. Mater. **13**, 139 (2014).
15. P. Genevet, F. Capasso, F. Aieta, *et al.*, "Recent advances in planar optics: from plasmonic to dielectric metasurfaces," Optica **4**, 139 (2017).
16. P. Chen, B. Y. Wei, W. Hu, *et al.*, "Liquid-crystal-mediated geometric phase: from transmissive to broadband reflective planar optics," Adv. Mater. **32**, 1903665 (2020).
17. Z. X. Xu, J. Chang, J. Y. Tong, *et al.*, "Near-field chiral excitation of universal spin-momentum locking transport of edge waves in microwave metamaterials," Adv. Photonics **4**, 046004 (2022).
18. A. U. R. Khalid, N. Ullah, Y. Han, *et al.*, "Single-layered non-interleaved spin-insensitive metasurfaces for wavefront engineering," Chin. Opt. Lett. **21**, 010006 (2023).
19. K. Achouri, V. Tiukuvaara, and O. J. F. Martin, "Spatial symmetries in nonlocal multipolar metasurfaces," Adv. Photonics **5**, 046001 (2023).
20. S. Slussarenko, A. Murauski, T. Du, *et al.*, "Tunable liquid crystal q-plates with arbitrary topological charge," Opt. Express **19**, 4085 (2011).
21. Y. Shen, X. Wang, Z. Xie, *et al.*, "Optical vortices 30 years on: OAM manipulation from topological charge to multiple singularities," Light Sci. Appl. **8**, 90 (2019).
22. Z. W. Jin, G. Y. Cao, H. T. Wang, *et al.*, "Broadband angular momentum cascade via a multifocal graphene vortex generator," Chin. Opt. Lett. **20**, 103602 (2022).
23. M. Rafayelyan and E. Brasselet, "Spin-to-orbital angular momentum mapping of polychromatic light," Phys. Rev. Lett. **120**, 213903 (2018).
24. J. B. Guo, F. Liu, F. J. Chen, *et al.*, "Realisation of cholesteric liquid-crystalline materials reflecting both right- and left-circularly polarised light using the wash-out/refill technique," Liq. Cryst. **37**, 171 (2010).
25. T. G. Lin, Y. D. Yuan, Y. Q. Zhou, *et al.*, "Bragg reflective polychromatic vector beam generation from opposite-handed cholesteric liquid crystals," Opt. Lett. **44**, 2720 (2019).
26. L. Zhu, C. T. Xu, P. Chen, *et al.*, "Pancharatnam–Berry phase reversal via opposite-chirality-coexisted superstructures," Light Sci. Appl. **11**, 135 (2022).
27. S. J. Liu, L. Zhu, Y. H. Zhang, *et al.*, "Bi-chiral nanostructures featuring dynamic optical rotatory dispersion for polychromatic light multiplexing," Adv. Mater. **35**, 2301714 (2023).
28. Y. K. Ji, X. Xie, L. Fang, *et al.*, "Cylindrical vector beam generator on photonic crystal cavity integrated with metal split ring nanoresonators," Chin. Opt. Lett. **21**, 033601 (2023).
29. D. W. Berreman, "Optics in stratified and anisotropic media: 4×4-matrix formulation," J. Opt. Soc. Am. **62**, 502 (1972).
30. Y. H. Huang, T. X. Wu, and S. T. Wu, "Simulations of liquid-crystal Fabry-Perot etalons by an improved 4×4 matrix method," J. Appl. Phys. **93**, 2490 (2003).
31. K. Eidner, "Light propagation in stratified anisotropic media: orthogonality and symmetry properties of the 4×4 matrix formalisms," J. Opt. Soc. Am. A **6**, 1657 (1989).
32. A. H. Gevorgyan, "Photonic band gaps from a stack of right- and left-hand chiral photonic crystal layers," Phys. Rev. E **85**, 021704 (2012).
33. Z. Q. He, K. Yin, and S. T. Wu, "Peculiar polarization response in chiral liquid crystal stacks for multispectral camouflage," Opt. Express **29**, 2931 (2021).
34. P. Yeh and C. Gu, *Optics of Liquid Crystal Displays* (John Wiley & Sons, 1999).
35. M. Tur, "Reflection at the boudary between glass and chloesteric liquid crystals," Mol. Cryst. Liq. Cryst. **29**, 345 (1975).
36. J. Kobashia, H. Yoshidaa, and M. Ozaki, "Broadband optical vortex generation from patterned cholesteric liquid crystals," Mol. Cryst. Liq. Cryst. **646**, 116 (2017).
37. M. Rafayelyan, G. Agez, and E. Brasselet, "Ultrabroadband gradient-pitch Bragg-Berry mirrors," Phys. Rev. A **96**, 043862 (2017).
38. R. Yuan, C. T. Xu, H. Cao, *et al.*, "Spin-decoupled transflective spatial light modulations enabled by a piecewise-twisted anisotropic monolayer," Adv. Sci. **9**, 2202474 (2022).